

EXIT PLANE H<sub>2</sub>O CONCENTRATION MEASUREMENTS CORRELATED WITH OH  
PLIF NEAR-INJECTOR MIXING MEASUREMENTS FOR SCRAMJET FLOWS

T.E. Parker, M.G. Allen, R.R. Foutter, D.M. Sonnenfroh, and W.T. Rawlins  
Physical Sciences Inc.  
Andover, MA 01810

## ABSTRACT

Mixing and combusting high enthalpy flows, similar to those encountered in scramjet engines, were investigated using a shock tunnel to produce the flow in conjunction with non-intrusive optical diagnostics which monitored the performance of two injector configurations. The shock tunnel is configured to produce Mach 3 flow and stagnation enthalpies corresponding to flight equivalent Mach numbers between 7 and 11. A pulsed hydrogen injection capability and interchangeable injector blocks provide a means of examining high speed, high enthalpy reacting flows. Planar Laser Induced Fluorescence (PLIF) of OH molecules in the near injector region produced images which show the combusting and mixing zones for the reacting flow. Line-of-sight exit plane measurement of water concentration and temperature were used to provide a unique method of monitoring exit plane products. These results demonstrated that a velocity matched axial injection system produced a fuel jet that lifted off the floor of the duct. Mixing was observed to increase for this system as a velocity mismatch was introduced. Comparison of exit plane water concentrations for a wall jet injection system and a velocity matched injection system indicated similar mixing performance but an accurate pressure measurement is necessary to further validate the result. In addition, exit plane measurements indicated an approximate steady-state condition was achieved during the 1 to 2 ms test times.

## INTRODUCTION

The development of supersonic combusting ram jet (SCRAMJET) engines requires testing using new, non-intrusive methods in high speed, high enthalpy flow facilities. A critical factor for effective thrust production in a scramjet is the efficient mixing of fuel with air and the subsequent chemical reactions which produce water. This paper describes an experimental effort which measured the concentration of water at the exit plane of a simulated scramjet in addition to using Planar Laser Induced Fluorescence (PLIF) of OH to visualize the mixing zone where hydrogen is injected into the Mach 3.0 flow. These results allow direct comparison of the degree of mixing near the hydrogen injector, as determined by the production of OH, with temperatures and concentration values for water 20 duct heights downstream of the injection station.

Results in this paper are for the initial development of a non-intrusive diagnostic for line-integrated temperature and concentration measurements of water. The observed quantity is infrared emission from the  $\nu_2$  vibrational band centered at 6.27  $\mu\text{m}$ , coupled with OH PLIF measurements in the near injector zone of a high enthalpy reacting flow. The flows were produced using a shock

tunnel which generates Mach 3.0 flow with stagnation conditions ranging from 2500 to 3800 K. Two hydrogen injector configurations were employed: a dual hole sonic wall injection system, and a swept ramp injector which was specifically designed to be nearly velocity matched with the mainstream flow. In addition to the water and OH PLIF measurements, exit plane emission from OH and entrance plane emission from NO were monitored. In the following sections we describe the shock tunnel and its operating characteristics, the injection system and its operating parameters, the OH PLIF measurements and methodology, the development of the water temperature and concentration measurement, and, finally, results from an initial test series with the two different injection geometries.

## SHOCK TUNNEL DESCRIPTION

A full description of the shock tunnel and its operation has been previously published.<sup>1</sup> Briefly, the high speed, high enthalpy flows for these tests were produced using a shock tunnel which is capable of generating stagnation temperatures far greater than those available using a conventional furnace or vitiated combustion methods. The facility also includes a hydrogen injection capability which makes combustion tests possible for these flows. This system was carefully designed to provide on-demand injection and can be configured to test a variety of injector geometries. The shock tunnel is configured to operate at Mach 3.0 with a two dimensional half-nozzle expanding to a square cross section. The nozzle is followed by a rearward facing step in the floor of the tunnel. A replaceable injector block lies immediately downstream of the isolation step. Five orthogonal optical access stations are included along the shock tunnel so that both line-of-sight and PLIF imaging measurements can be made. The first optical port is immediately after the full expansion point for the nozzle and includes three windows. The first three windows are shown schematically in Figure 1 along with the interchangeable injector block. The region immediately after the rearward facing step includes two side windows that give full height optical access for a 14 cm flow length, along with full laser access at the top of the tunnel.

Figure 2 illustrates the shock tunnel and diagnostics as configured for this test series. Four distinct optical measurements were included. In addition to OH PLIF and water vapor emission measurements, a radiometer centered at  $4.95 \mu\text{m}$  was included at the nozzle exit and a gated intensified camera filtered to monitor the OH chemiluminescent emission was included at the exit plane. The upstream radiometer was used to monitor the flow in the tunnel via emission from the NO fundamental vibrational band as described in a separate publication<sup>2</sup>. This measurement is critical in determining the test conditions for the shock tunnel since it provides a signal from the thermal emission from NO generated in the plenum. Measurable emission signals are only present when the flow in the tunnel is at the elevated temperatures produced by the reflected shock zone. This measurement is therefore much more specific in determining the tunnel test times than conventional pressure measurements. A critical performance parameter for impulse test facilities, such as a shock tunnel, is the time duration of the high enthalpy flow. Test times determined using the previously described radiometer were typically between 1 and 2 ms.

The shock tunnel is used to produce the very high stagnation conditions associated with supersonic/hypersonic flight. Figure 3 illustrates the flight simulation capabilities for the shock tunnel compared with a flight corridor adopted by Billig<sup>3</sup>. Clearly the shock tunnel is capable of

simulating flight speeds below 3 km/s in the lower pressure regions of the flight corridor. Also included in this figure is the testing region examined in this work. Flight equivalent Mach numbers ranged from 7 to 11.

## HYDROGEN INJECTION SYSTEM AND INJECTOR CONFIGURATIONS

To produce reacting flows similar to those in a scramjet, hydrogen must be injected into the shock tunnel flow. The requirements for this are pulsed operation with a fast response time, near constant injection flow rates during the shock tunnel run time, and a reliable method of limiting the quantity of hydrogen injected into the system. We have addressed these requirements using a 1 gal, 3000 psi rated bladder accumulator with a custom manufactured, explosive burst diaphragm and manifold system. A dual diaphragm system separates the nitrogen pressurized hydrogen from the delivery system for the injector block. Injection is possible on demand by simply igniting a hydrogen/oxygen mixture contained between the diaphragms with a spark plug. Testing of this system revealed that initiation times of 800  $\mu$ s were routinely produced. The injection system can therefore be triggered using one of the pressure transducer signals from the shock tube.

The overall stoichiometry for the combustng system can be easily described since the injectors in the combustion zone are configured to produce sonic flow at a known area. Using standard gasdynamic relationships, the product of injection pressure and injector exit hole area can be shown to be a function of system stoichiometry and reflected shock temperatures and pressures, Eq. (1).

$$P_{O,H_2} A_{inj} = \phi \frac{P_5}{\sqrt{T_5}} K_1 \quad (1)$$

where

- $P_{O,H_2}$  - stagnation injection pressure
- $A_{inj}$  - injector sonic area
- $\phi$  - fuel equivalence ratio
- $P_5, T_5$  - reflected shock plenum pressure and temperature
- $K_1$  - system constant,  $2.12 \times 10^{-3} \text{ m}^2\text{-K}^{1/2}$ .

This equation was derived by considering the ratio of mass flows through the shock tunnel nozzle throat and the mass flow at the sonic exit point of the fuel injection system. Using this equation, a specific heat ratio of 1.3 for the air flow, and recognizing that an equivalence ratio of 1.0 corresponds to a mass ratio, hydrogen to air, of 0.029, Eq. (1) may be constructed. The system constant,  $K_1$ , includes the area of the shock tunnel throat as well as the various constants used to relate one-dimensional sonic flow to the zero velocity plenum conditions.

The two injector configurations used in this work are illustrated in Figures 4 and 5. The wall injection system consists of two ports located in the tunnel floor after the rearward facing step,

along the tunnel centerline, at 2.3 and 8.4 step heights downstream. The equal area inlets are directed at 30 and 60 deg angles with respect to the tunnel flow. The axial injection system was implemented by lengthening the step across the full tunnel width. This addition was sectorized into three equal widths with the outer sectors machined to produce a 13.2 deg ramp between the step and the tunnel floor. The center sector consists of a backward facing step with a nozzle in the downstream face. This nozzle was a simple 7 deg taper with a throat area of  $0.317 \text{ cm}^2$  and an exit area ratio of 3.2. This system was specifically designed to produce bulk and injection flow velocities of approximately equal magnitude. Table 1 lists relevant velocities and stoichiometries for four of the conditions examined in this work.

## OH PLIF MEASUREMENTS

The OH PLIF measurements were made using a Spectra-Physics Nd:YAG-pumped dye laser with frequency-doubling to 283 nm. The dye laser was modified for a larger spectral bandwidth by operating the grating in third order rather than fifth and adding a pre-amplifier cell. Using this approach, the frequency-doubled output of the dye laser was in excess of  $0.6 \text{ cm}^{-1}$ , more than twice that of the OH absorption linewidth. Between 6 and 10 mJ of laser energy was delivered to the test plane of the shock tunnel in sheets of 4.5 to 10.5 cm. The laser sheet thickness was on the order of 0.05 cm. Fluorescence was imaged using an intensified camera system, consisting of an image-intensified full-frame transfer array. The fluorescence was collected at right angles using a 105 mm UV lens operated at  $f/4.5$  and filtered with carefully selected UV filter glasses. The filter glasses provided a long-pass cut-off near 310 nm which rejected the laser elastic scattering from the tunnel floor. The total transmission at the fluorescence wavelengths was about 25%. The intensifier was gated to  $\sim 20 \text{ ns}$  around the  $\sim 10 \text{ ns}$  laser pulse. This narrow gate width eliminated any chemiluminescent or thermal emission from the PLIF images.

The laser and PLIF data acquisition system were remotely sited from the tunnel in an adjacent laboratory. The laser beam was transported to the tunnel using a series of prisms and expanded into a thin sheet which was oriented along the flow axis and focussed along the centerline of the tunnel at each of the imaging stations. The intensified camera system and the high-speed gate generator were located immediately adjacent to the tunnel test section. The laser and camera system were triggered from a pressure transducer in the reflected-shock plenum so that the measurement time could be adjusted throughout the nominally 2 ms test time. OH PLIF measurements were made in the near field of both injector configurations, spanning the first region of the test section downstream of the rear-facing step or the ramp injector, as well as at a second imaging station located downstream of the test section entrance.

In addition to the OH PLIF measurements, a second, PSI-designed, intensified CCD camera was used to image the OH chemiluminescence from a 10 cm diameter window located near the exit of the tunnel test section. For the emission measurements, the second camera was filtered with 3 mm of UG-5 glass to isolate the OH A-state emission, and a  $1 \mu\text{s}$  gate was used. This longer gate time integrated the emission signal which was eliminated from the PLIF images by the much shorter gate time. The depth-of-focus of the emission-imaging camera was sufficient to span the 7.62 cm tunnel width, providing a line-of-sight averaged view of the spreading of the flame plume at the test section exit.

The OH PLIF measurements were obtained by exciting the isolated  $Q_1(7)$  transition at 283.29 nm. This transition was chosen because of its strength at the expected  $H_2$ -air combustion temperatures and our desire to have maximum sensitivity for these experiments. For the conditions of these tests, we may express the fluorescence signal obtained from each pixel on the detector array as

$$S_F = (I_\nu B) \cdot (F_y) \cdot (f_B N_t V_c) \cdot \left[ \eta \frac{\Omega}{4\pi} \right] \cdot \tau_p \quad (2)$$

where

$I_\nu$	=	laser spectral intensity
$B$	=	Einstein B coefficient for absorption
$F_y$	=	fluorescence yield
$f_B$	=	Boltzmann population fraction
$N_t$	=	species number density
$V_c$	=	collection volume
$\eta$	=	filter transmission, detector responsivity, etc.
$\Omega$	=	collection solid angle of imaging system
$\tau_p$	=	pulse duration.

The form of the fluorescence yield,  $F_y$ , appropriate for this excitation strategy in OH is given by<sup>4</sup>

$$F_y = \frac{A_{eff}}{Q} \quad (3)$$

where  $Q$  is the total rate of removal of the laser-excited vibrational level,  $A_{eff}$  is the total collected photon rate and the sum of the product of the filter transmission and the individual spontaneous radiative transition rates for the detected transitions.

In general, many of the terms in Eq. (2) have temperature, pressure, or gas compositional dependencies. For OH in most flame environments, it is reasonable to assume that the quenching term can be expressed as

$$Q = (8 \times 10^8) (P/P_{ref})^{-1} \quad (4)$$

where  $P_{ref}$  is 1 atm and the constant is recommended for flame values from previous studies.<sup>5-8</sup> Hence, in regions of the flow with little pressure variation across the measurement plane, as in the downstream PLIF imaging station, the quenching term is essentially constant and the PLIF image is a relative measure of the product of the OH number density and the temperature-dependent Boltzmann population term. For  $J'' = 7.5$ , the population term is only weakly sensitive to temperature over the range of temperatures where OH is likely to be found, as shown in Figure 6. The quenching term may vary as much as a factor of two from the nominal value of Eq. (4) in extremely fuel rich portions of the flow. However, most of the measurable OH will only be found in stoichiometric or fuel-lean regions of the flow, so that we can assume the relative uncertainty in number density across a nearly constant pressure image is about  $\pm 10\%$  due to the Boltzmann temperature variations.

In strongly pressure variant flows, however, the fluorescence signal is better viewed as the ratio of the pressure-dependent OH number density and the pressure-dependent quenching term. Expressing  $N_{OH}$  as

$$N_{OH} = \chi_{OH} P/RT \quad (5)$$

where  $\chi_{OH}$  is the volumetric mole-fraction of OH, the overall pressure-dependence of Eq. (2) vanishes, and the fluorescence signal is given by

$$S_F = \text{constant} \cdot f_B/T \cdot \chi_{OH} \quad (6)$$

Since the Boltzmann term at low  $J''$  values is nearly temperature-independent, the ratio  $f_B/T$  is an inverse function of temperature and is also plotted in Figure 6. Hence, the fluorescence signal is proportional to the local mole-fraction of OH with a factor of four variation from 1500 to 3000 K. It is possible to choose another transition so that the ratio  $f_B/T$  is essentially constant over some temperature range of interest so that, in strongly pressure varying flows, the fluorescence signal is directly proportional to species mole-fraction. For the range of 1500 to 3000 K, exciting transitions originating from higher  $J''$  values results in about  $\pm 5\%$  variation in fluorescence at constant mole-fraction with only a factor of two loss in sensitivity at 2000 K due to the relatively lower total population. For these initial measurements, the increased sensitivity was deemed more important and we chose to accept the temperature variations in the strongly pressure-variant region of the flow in the vicinity of the dual wall injectors.

## MEASUREMENTS OF H<sub>2</sub>O CONCENTRATION AND TEMPERATURE

A major thrust for this work was to develop a non-intrusive diagnostic suitable for monitoring the temperature and concentration of water in the exit plane of a high enthalpy reacting flow system. The motivation for this measurement technique is quite clear; it will provide a direct measure of a combustion product and its temperature along a line-of-sight at the combustor exit and will therefore provide a measure of combustor performance. The measurement relies on radiation from the  $\nu_2$  band centered at 6.27  $\mu\text{m}$  and uses a custom-designed infrared spectrometer system capable of acquiring synchronous spectra at a 125 kHz rate. This device consists of a liquid-nitrogen-cooled HgCdTe linear detector array (Infrared Associates) interfaced to a 0.3m,  $f/6.2$  monochromator. The resulting spectral resolution is 0.19  $\mu\text{m}/\text{pixel}$ . Each pixel in the array has a dedicated amplifier and digitizer providing synchronous collection of spectra at data rates of 125 kHz. The data were acquired and processed through a multichannel data acquisition system interfaced to an PC/AT computer. Absolute responsivity calibrations were performed with a temperature-controlled blackbody source. For the present measurements, the instrument was configured to obtain time-resolved, first-order spectra over the wavelength range 6.5 to 8.55. The field of view of the instrument was controlled using a folded imaging system consisting of a gold spherical mirror (focal length 10 cm) and a gold planar mirror. This optical system defined a collection area in the tunnel of 3.1 by 3.1 mm at the tunnel centerline and 6.6 by 6.6 mm at the near and far edges. In addition, due to the strong absorption strength of atmospheric water in this spectral region, the spectrometer and imaging optics assembly were purged with dry nitrogen. The unpurged path length in the atmosphere was 7 cm and this length was shown to produce insignificant

absorption for wavelengths greater than 6.5  $\mu\text{m}$ . This conclusion is supported by a comparison of the spectrometer calibrations performed in high and low relative humidity environments.

Prior to implementation of the system on the shock tunnel, the observed radiances and bandshapes were calibrated for  $\text{H}_2\text{O}$  concentration and temperature by recording emission spectra from an incident shock heated mixture of argon, hydrogen, and oxygen (85%, 10%, 5%). The measurements were performed at near 1 atm pressures in a 10.4 cm diameter shock tube using previously prepared gas mixtures of UHP argon, hydrogen, and oxygen. The reacting system is modeled using an incident shock chemical kinetics package produced by Sandia (DSHOCK), and calibration temperatures and concentrations are carefully extracted from the pseudo-steady state region following an initially reactive period. A typical calibration shock is shown in Figure 7.

Relative calibration spectra are shown in Figure 8 and these spectra show the increased radiance for long wavelengths at elevated temperatures that is typical of increased populations in upper vibrational states. The vibrational temperature for the water can therefore be determined by monitoring the relative shape of the emission spectra while the concentration is determined by monitoring the absolute radiance in one of the bandpasses. In order to produce a systematic temperature and concentration measurement methodology we have assumed that the radiance in each bandpass follows the functional form given in Eq. (7).

$$\frac{N_\lambda}{[\text{H}_2\text{O}]\ell} = \alpha_\lambda e^{\beta_\lambda/T} \quad (7)$$

where

- $N_\lambda$  - system radiance at wavelength  $\lambda$
- $[\text{H}_2\text{O}]$  - concentration of water molecules
- $\ell$  - path length
- $T$  - temperature
- $\alpha_\lambda, \beta_\lambda$  - empirically determined constants.

The characteristic exponential slope  $\beta_\lambda$  increases with wavelength as would be expected from the spectra shown in Figure 8. Inspection of Eq. (7) reveals that ratios of radiances at two wavelengths are sensitive to temperature only and are independent of concentration. Equation (8) formalizes this relationship and provides a direct means of calculating temperature. The values of  $\alpha_\lambda$  and  $\beta_\lambda$  are determined using a least squares fit of the calibration observations to Eq. (7). Therefore, observed radiance ratios can be used to determine the temperature via Eq. (8) and column density ( $[\text{H}_2\text{O}]\ell$ ) using Eq. (7).

$$T = \frac{\beta_{\lambda_1} - \beta_{\lambda_2}}{\ln \left[ \frac{N_{\lambda_1} \alpha_{\lambda_2}}{N_{\lambda_2} \alpha_{\lambda_1}} \right]} \quad (8)$$

The specific bandpass wavelengths which are used for temperature and concentration determination is important for the shock tunnel data. Figure 9 illustrates sample spectra at the exit

plane of the shock tunnel for a combusting flow. These spectra include a feature centered at 8.25  $\mu\text{m}$  which was not apparent in the shock tube calibrations. This feature is either due to a molecular radiator that was not present in the shock tube calibrations (which included no nitrogen) or is indicative of vibrational non-equilibrium for the radiating water. Although we cannot rule out vibrational non-equilibrium, vibrational relaxation rates from  $\nu_2 = 1$  to  $\nu_2 = 0$  are relatively fast.<sup>9</sup> For 2500 K, 0.3 atm conditions in the tunnel, the half-life of the  $\nu_2 = 1$  state is approximately 7 ns. This indicates that our system should be in vibrational equilibrium. In either case, we have chosen to determine temperature using the bandpasses centered at 6.68 and 7.43  $\mu\text{m}$ . Concentration is determined using this temperature and the radiance from 6.68  $\mu\text{m}$  bandpass. These bandpasses were selected to provide the highest sensitivity in the temperature calculation while the concentration calculation was specifically chosen to be insensitive to temperature.

Finally, a note on the accuracy of the temperature and concentration measurement is in order. This diagnostic is currently being developed and the calibration data set is not large enough to produce system constants that are highly specified. The absolute accuracy for the current data set is approximately 30%. However, careful implementation of a comprehensive calibration matrix and carefully executed chemical kinetic modeling would bring the absolute accuracy to better than 10%. Once these calibration constants are accurately specified, the limiting accuracy for the temperature measurement is simply the signal-to-noise ratio in the radiance measurements. The direct implication is that temperature *comparisons* within this data set are limited only by the noise in the radiometric signals. In all cases, the signal levels used in this work had signal-to-noise ratios of between 10 and 50. The relative uncertainty in temperature is therefore between 14 and 3%, while the relative uncertainty in concentration for a 3000 K system also ranges from 14% for signal to noise ratios of 10 to 3% and for signal-to-noise ratios of 50.

## RESULTS AND DISCUSSION

The data acquired as a part of this test series includes four basic flow conditions as described in Table 1 and we will present results from each of these conditions. However, before discussing these images and the exit plane water measurements, a brief discussion of the flow and timing in the shock tunnel is necessary. Figure 10 illustrates the signals from a reacting flow test and shows the pressure in the injector plenum, the signal from the radiometer at the nozzle exit, and the pressure on the top wall immediately following the injector station. Also included in this figure are the injector times and PLIF laser pulse. Features to note in this figure are the clear demarcation of the flow test time by the radiometer, the relatively stable pressure trace following the injector station, and the constant pressure in the injector plenum during the flow time. In addition, note that tunnel pressure and radiance signals are not coincident in space (separation is 0.30m) and therefore sample, at a given instant, different portions of the flow.

Figure 11 is an image of the OH distribution in the immediate vicinity of the first injector of the dual injector system. In this and all other images, the flow is from left to right and the relative fluorescence signal levels are false-color-encoded according to the lookup table at the left side of the image. Also in each image, the bottom of the PLIF image corresponds to the bottom wall of the tunnel. The field of view in Figure 11 is 80 mm (H) by 60 mm (V) and the left side of the image is just upstream of the first injector. A low, fairly uniform level of OH in the recirculation

zone/boundary layer upstream of the injector is visible in the lower left hand corner of the image. A thin filament of OH, on the order of 1 mm thick, attaches very near the recirculation zone and extends away from the wall along an irregular line, indicative of the shear-generated turbulence between the high-speed injectant flow and the free-stream flow. From earlier studies<sup>4</sup>, we know that just upstream of this OH zone lies the bow shock generated by the interaction of the injectant plume and the free stream flow. The dark regions above this thin filament, of course, correspond to the free-stream flowfield where no hydrogen and air mixing has occurred. The center of the fuel plume itself is also dark, indicating no mixing and OH formation. Downstream and underneath the fuel plume, between the two injectors along the tunnel floor, significant amounts of OH are observed in a spatially extended, reasonably well-mixed zone.

Figure 12 is a similar image from another test, now taken with a larger field of view, observing a region 105 by 79 mm. Again, the left side of the image is just upstream of the first injector position. This image also clearly shows the thin OH filament between the first injector and the free stream flow. The large field of view, however, encompasses the second injector station and more clearly shows the large, well-mixed levels of high OH concentration between the two injectors. The right side of this image corresponds to the second injector station and shows an abrupt disappearance of the OH at the second H<sub>2</sub> plume, although a second thin filament is observable at a larger angle to the wall than the first filament due to the higher angle of the second injector. Both images indicate that the thin OH filament is typically on the order of 1 mm thick, although it fluctuates spatially with the turbulence motion in observable scales up to about 7 mm in diameter. The first jet penetrates to an average height of 16 mm (defined by the edge of the OH filament) before fully aligning with the free stream flow.

Using the fluorescence model presented above and assuming nominal conditions of 0.5 atm and 2000 K, the peak OH fluorescence signal in the thin filament between the fuel jet and the free-stream corresponds to an OH number density of about  $1 \times 10^{15} \text{ cm}^{-3}$ , or about 500 ppm. The pressure and temperature field in this portion of the flowfield is very complex. The nominal conditions are reasonable for the OH in the filament above the fuel jet. Below the fuel jet and between the two injectors, however, the flow expands from a stagnation point upstream of the first injector and then stagnates again upstream of the second injector. Since we have not yet measured the pressure or temperature variations in this flow, we can only bound the uncertainty in quantitatively interpreting the relative fluorescence signals in this image in terms of the relative OH number density or mole-fraction. The pressure in this region may vary from near the free stream value to near the post-bow shock pressure, or from about 0.5 to about 4 atm. The temperature in which OH is likely to be found was discussed in the previous section and we observe that, in the stagnation region upstream of the second injector station, the bulk gas temperature may approach the stagnation temperature of  $\sim 3500 \text{ K}$ .

The highest fluorescence signals originate in the large, well-mixed portion of the flow where the flow temperatures and pressures are substantially higher than the nominal conditions used to estimate the OH concentration in the flame filament. The peak signal levels here are two to three times higher than in the filament. Considering the mole-fraction sensitivity of the fluorescence signal (which is independent of pressure), we expect the fluorescence signal at constant mole-fraction to decrease by about a factor of two from the nominal filament temperature to the stagnation temperature. Combining the increased signal levels and the decreased absorption strength at higher temperature, we estimate that the peak mole-fractions obtained in the region between the two

injectors is on the order of 2,000 to 3,000 ppm, or 0.2 to 0.3% of the total number density. These numbers are reasonable for hydrogen/air combustion at these temperatures, particularly considering the relatively long residence time for the fuel and air to molecularly mix in the slow flow between the injectors.

The flame zone in the upper filament, as viewed by the OH fluorescence, is intermittent. Our detection limit for the nominal conditions is about  $1 \times 10^{13} \text{ cm}^{-3}$ , or about 5 ppm. Hence, intermittency is determined in this case by the OH concentration falling below this level. This type of non-equilibrium flame extinction has been observed in turbulent hydrogen/air jet diffusion flames and is reasonably expected in the highly turbulent flow in the injector vicinity. The PLIF images of Figures 11 and 12 indicate the importance of time-resolved spatial measurements and suggest that accurate predictions of ignition and near-injector behavior will require multi-step chemical kinetic and accurate turbulence modeling.

The remaining PLIF images all correspond to the axial injector and were obtained 29 cm downstream of the injector exit plane. Figure 13 is a PLIF image at the similar flow condition to Figures 11 and 12 and corresponds to a field of view of 45 by 34 cm. In these images, the injectant hydrogen velocity was nearly matched to the free stream centerline velocity above the injector. The OH filament separating the fuel jet from the free stream is typically on the order of  $500 \mu\text{m}$  thick, although it fluctuates spatially due to the turbulence in the shear layer. This turbulence level is relatively low, however, as evidenced by the thin, probably diffusion limited flame sheet and the relatively large scale associated with the typical filament fluctuations. It is also notable that no extinction of the flame sheet is observed. The dark region below the flame sheet corresponds to the fuel jet itself, which measures approximately 12 mm in diameter, essentially the same as the injector jet diameter. The position of this jet above the tunnel flow, however, fluctuates with downstream distance. The mean position of the jet centerline is about 20 mm.

In marked contrast to the interface between the fuel jet and the free stream, the region between the fuel jet and the wall shows a much thicker mixing layer. Significant free stream air entrainment and mixing is evidenced by the large, relatively uniform [OH] in this region. The picture that emerges from this image is of a fuel jet lifting away from the wall and vigorously mixing underneath. The peak OH levels in these images are again on the order of  $2\text{-}3 \times 10^{15} \text{ cm}^{-3}$ . Since the pressure across this image is reasonably constant, we can more accurately relate the fluorescence signal variations to number density variations than in the images above the side wall injectors. Interestingly, the OH formation per unit volume is similar everywhere in this image to the thin filaments above the side wall injectors, although the total OH produced in the image (proportional to the total hydrogen conversion) is much greater due to the vigorous mixing below the jet.

Figure 14 is an OH PLIF image at the same station with a different field of view and flow conditions as given in Table 1. In Figure 14 the field of view was increased to  $60 \times 45 \text{ cm}$  and the velocity difference between the fuel jet and free stream was nearly 300 m/s (the fuel jet velocity is greater than that of the free stream). This image reveals a very different mixing pattern for the fuel jet. Instead of a clearly defined fuel jet with a thin filament separating the jet from the free stream, vigorous mixing has occurred on both sides of the jet. Indeed, the jet itself is almost indistinguishable, with measurable OH throughout its diameter. The penetration of the fuel jet into the free stream is slightly diminished although the mixing and total OH formed within the image is substantially higher. The sensitivity in these images is the same as in Figures 12 and 13 indicating

peak concentrations on the order of  $10^{15} \text{ cm}^{-3}$ . It is interesting to note that the increased turbulence intensity of the fuel jet/free stream shear layer now results in intermittency of the flame sheet.

A last PLIF image was obtained at the same location, now with the free-stream gas temperature over 1500 K and a velocity over 2000 m/s. In this case, the free-stream velocity slightly exceeds the expected fuel jet velocity, though the total velocity mismatch is comparable to that in Figure 14. The OH PLIF image in Figure 15 reveals a mixing pattern very similar to that of Figure 13, although the highest signal levels are now in the thin filament between the fuel and the free stream rather than between the fuel and the wall. The penetration of the jet into the free stream is noticeably improved, with the outer OH boundary extending 34 mm above the tunnel floor.

Figures 16 and 17 show the results from the time resolved,  $\text{H}_2\text{O}$  temperature and concentration measurements. These results are for the wall injection system and swept ramp injector at similar flow conditions as listed in Table 1. Figure 16 illustrates the temperature and column density profiles for the two hole wall injection system. This plot uses the 125 kHz spectral data which was previously described with a three point running average to remove spurious noise. Several features are prominent in this figure. First, the end of the test time is clearly shown by a steep drop in the temperature of the water. The length of the test time, as defined by the infrared radiometer at the nozzle exit, is used to identify the beginning of the flow time at this optical station. This time is consistent with the expected arrival time of the hot gas slug based on the distance between the measurement stations and convective velocity in the tunnel. This figure is also marked to note the region where the signal-to-noise ratios rise above the 10:1 level. Both temperature and column density start at relatively low values and after approximately 1 ms asymptote to relatively steady conditions. This is an important observation since it supports the hypothesis that pulsed, short duration flow facilities can be used to study the steady state properties of these high temperature reacting flows. The observed exit plane temperature is approximately 2700 K with a column density of  $4\text{-}5 \times 10^{18} \text{ molec/cm}^2$ .

Figure 16 also includes idealized temperature and column density predictions. These predictions are based on a simplified model which creates an initial, fully mixed starting condition based on the air and hydrogen injection flows and then allows this system to react as it flows down the duct. This prediction follows the temperature, pressure, species concentrations, and velocity as the system proceeds down the duct. The starting condition for this calculation is determined by specifying a completely homogeneous system with the pressure, temperature, and velocity imposed by conserving mass, momentum, and enthalpy from the inlet air and hydrogen flows (note that the momentum of the hydrogen for the wall injection system was neglected since it was not oriented in the downstream direction). The initial chemical composition is chosen to reflect the exit composition of the air and hydrogen flows. Results from these calculations provide a relevant comparison for the exit temperature and column density measurements. In all of the experimental cases, the agreement between predicted and observed temperatures was excellent. However, the agreement in predicted and measured column densities is less consistent.

The column density observed in Figure 16 was approximately 60% of the idealized value. This discrepancy could be due to either incomplete mixing and therefore incomplete product formation, finite rate chemistry which would slow the rate of product formation, variations in the composition of the exit plane, or heat transfer losses in the system which will act to decrease the

density and therefore the water concentration. Unfortunately, our measurements for this effort did not include reliable pressure measurements at the exit plane. In all cases, pressure measurements are clearly biased by a heating of the piezo electric transducer which produces a continuous drift in the pressure signal during the experiment. In the future, this problem will be corrected by recessing the transducer from the flow so that it will not be directly subjected to the high temperatures and velocities of the exit plane.

Figure 17 illustrates the results for an axial injection system operated at conditions identical to that for Figure 16 (wall injection system). The observed column density for this system is very similar to that observed for the wall injector. In each of the two cases the observed column density was approximately 60% of their observed idealized values which preliminary indicates that the mixing of the velocity matched swept ramp system was equivalent to that of the wall injection system. If the mixing for one of the systems was exceptionally poor, the result would be decreased water in the exit plane of the combustor. Unfortunately this conclusion must be tempered by the absence of a pressure measurement which would allow a complete comparison between the two data sets. However, it is encouraging that the results for the velocity matched axial system and the wall injection system are similar.

## CONCLUSIONS

Complementary non-intrusive diagnostic measurements have been used to study the operation and performance of two different types of injection systems in high enthalpy flows. Planar Laser Induced Fluorescence of OH was used to image the regions near the injectors and a line-of-sight emission measurement in the infrared was used to quantify the temperature and the column density of water at the exit plane centerline. A fast gating, intensified camera system was shown to effectively eliminate emission from the fluorescence images. The exit plane emission measurement monitored the radiance from the  $\nu_2$  band for water. Relative band shape was used as a measure of temperature and the absolute intensity as a measure of the column density. PLIF images of OH for a wall injection system indicated prompt ignition at the hydrogen outlet with a flame sheet which attaches to the recirculation zone and extends away from the wall along an irregular line. An intense reaction zone was clearly shown to exist between the first and second fuel jet. For the axial injection system, OH was not observable immediately downstream of the injector outlet. However, further downstream, the fuel jet was shown to be reacting vigorously with the free stream flow. The axial injector was tested in both a velocity matched and mismatched mode. In all cases the jet was observed to lift off the tunnel floor with a reaction zone forming between the jet and the tunnel floor. In addition, the character of the mixing zone for the swept ramp systems was shown to change dramatically between velocity matched and mismatched systems. Exit plane measurements of the temperature were in excellent agreement with the values predicted for these flows. In addition, exit plane measurements indicated an approximate steady-state condition was achieved during the 1 to 2 ms test times.

## ACKNOWLEDGEMENTS

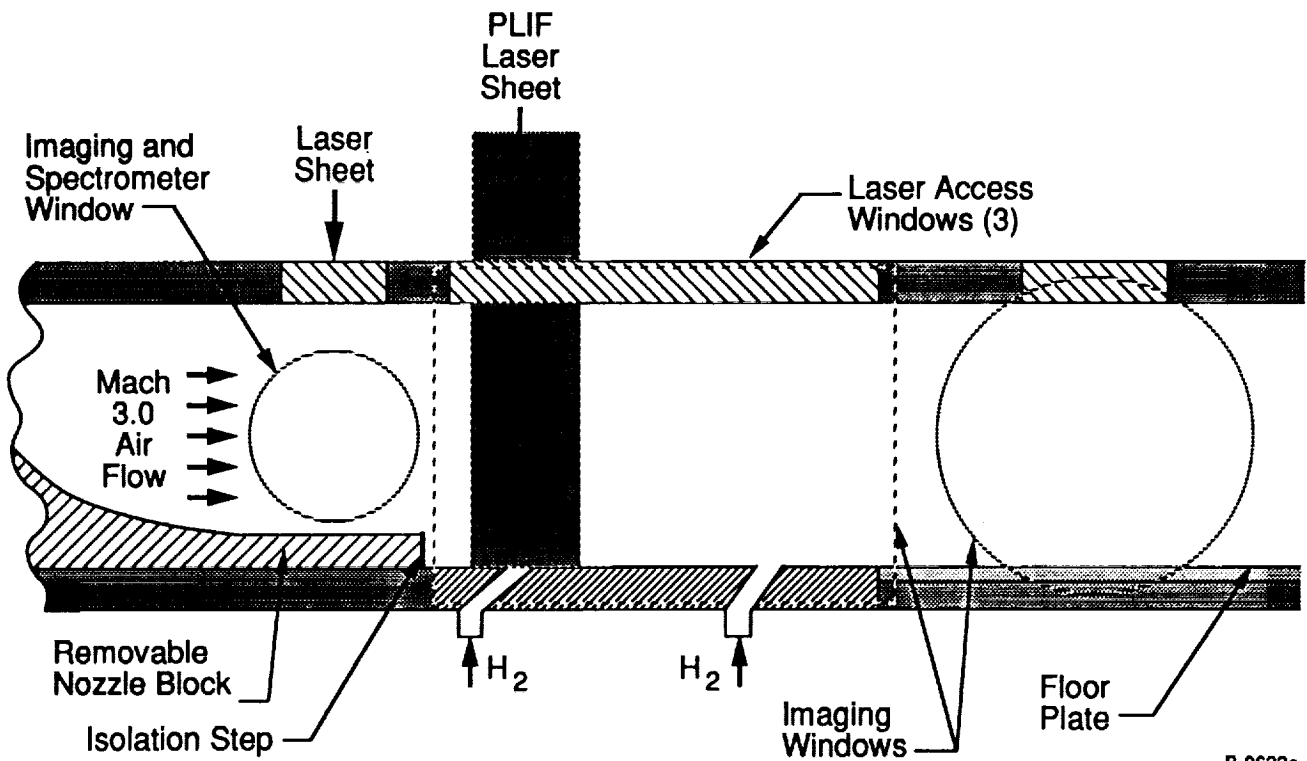
This work was supported by the Air Force under Contract F33615-91-C-2204, Dr. Kervyn Mach, monitor. We also appreciate our discussions with Dr. G. Burt Northam of NASA Langley on fuel injection geometries.

## REFERENCES

1. T.E. Parker, M.G. Allen, W.G. Reinecke, H.H. Legner, R.R. Foutter, and W.T. Rawlins, Paper No. 92-0761, AIAA 30th Aerospace Sciences Meeting and Exhibit, January 1992.
2. W.T. Rawlins, T.E. Parker, R.R. Foutter, and M.G. Allen, "Path Averaged Number Density and Temperature in High Enthalpy, Supersonic Air Flows by Time-Resolved Infrared Emission Spectroscopy," Paper No. 92-0140, AIAA 30th Aerospace Sciences Meeting, January 1992.
3. F.S. Billig, "Current Problems in Non-Equilibrium Gas Dynamics SCRAMJET Engines," presented at AIAA Professional Study Seminar on Gas Dynamics, Buffalo, NY, June 1989.
4. M.G. Allen, T.E. Parker, W.G. Reinecke, H.H. Legner, R.R. Foutter, W.T. Rawlins, and S.J. Davis, "Instantaneous Temperature and Concentration Imaging in Supersonic Air Flow Behind a Rear-Facing Step with Hydrogen Injection," Paper No. 92-0137, AIAA 30th Aerospace Sciences Meeting, January (1992).
5. G.P. Smith and D.R. Crosley, "Vibrational Energy Transfer in  $A^2\Sigma^+$  OH in Flames," *App. Opt.* **22**(10), 1428 (1983).
6. N.L. Garland and D.R. Crosley, "On the Collisional Quenching of Electronically Excited OH, NH, and CH in Flames," *21st Symposium (Int.) on Combustion* (Pittsburgh: The Combustion Institute), 1693 (1986).
7. M.C. Drake and R.W. Pitz, "Comparison of Turbulent Diffusion Flame Measurements of OH by Planar Fluorescence and Saturated Fluorescence," *Experiments in Fluids* **3**, 283 (1985).
8. R.S. Barlow and A. Collignon, "Linear LIF Measurements of OH in Non-Premixed Methane-Air Flames: When Are Quenching Corrections Unnecessary," Paper no. 91-0179, AIAA 29th Aerospace Sciences Meeting, January (1991).
9. P.F. Lewis and D.W. Trainor, "Survey of Vibrational Relaxation Data for  $O_2$ ,  $N_2$ , NO,  $H_2$ , CO, HF, HCL,  $CO_2$ , and  $H_2O$ ," Advanced Research Projects Agency Report No. 1092 (1974).

Table 1. Injection and Flow Parameters

Injector	Tunnel Flow			Fuel Equivalence Ratio	Injector Velocity (m/s)	OH PLIF Image Figure #	H <sub>2</sub> O Exit Plane Figure #
	Velocity (m/s)	Pressure (atm)	Temperature (K)				
Wall	2120	0.27	1310	2.1	-	11	-
Wall	2170	0.29	1360	2.1	-	12	16
Axial	1930	0.68	1100	0.64	2270	14	0
Axial	2184	0.30	1375	1.82	2270	13	17
Axial	2330	0.40	1530	1.35	2270	15	-



B-9622a

Figure 1. Schematic diagram of optical access for the shock tunnel test section

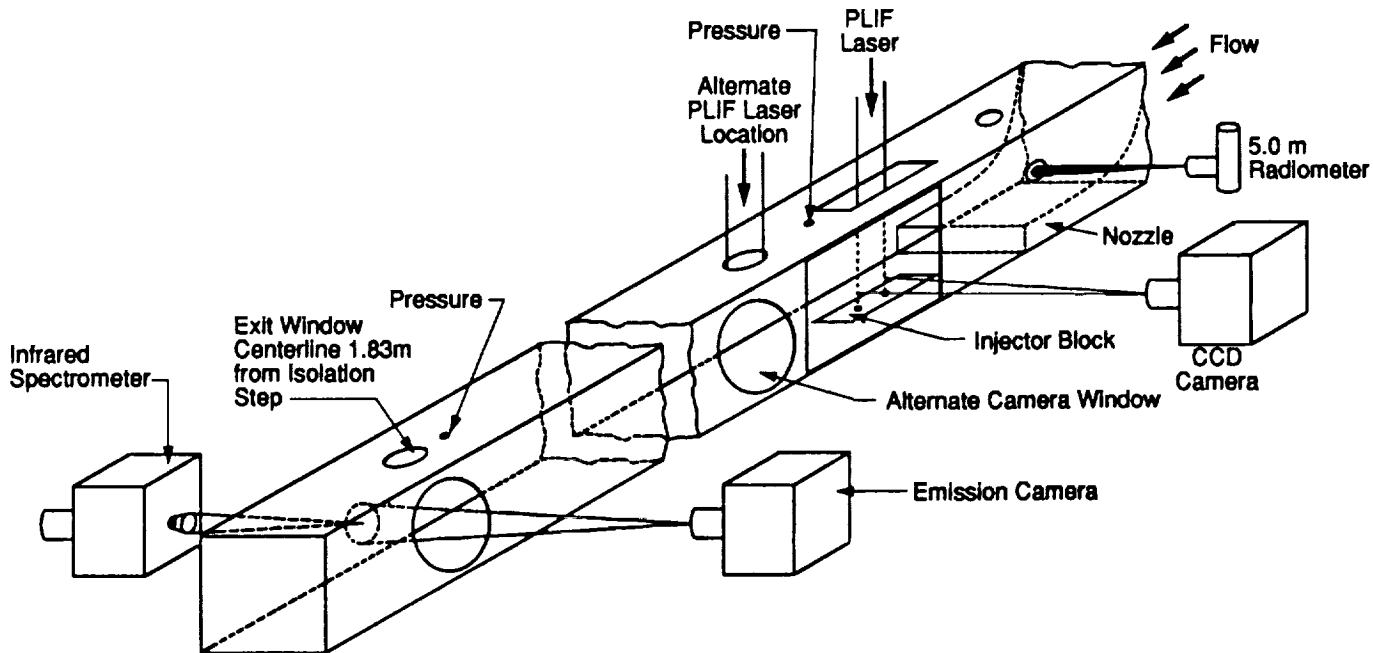


Figure 2. Diagnostic setup for reacting flow tests

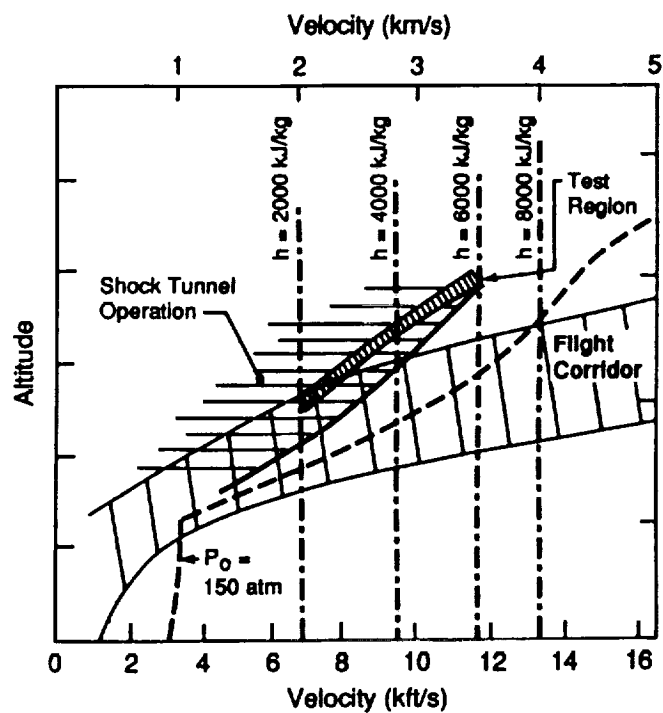


Figure 3. Shock tunnel operating conditions in terms of altitude and velocity simulation

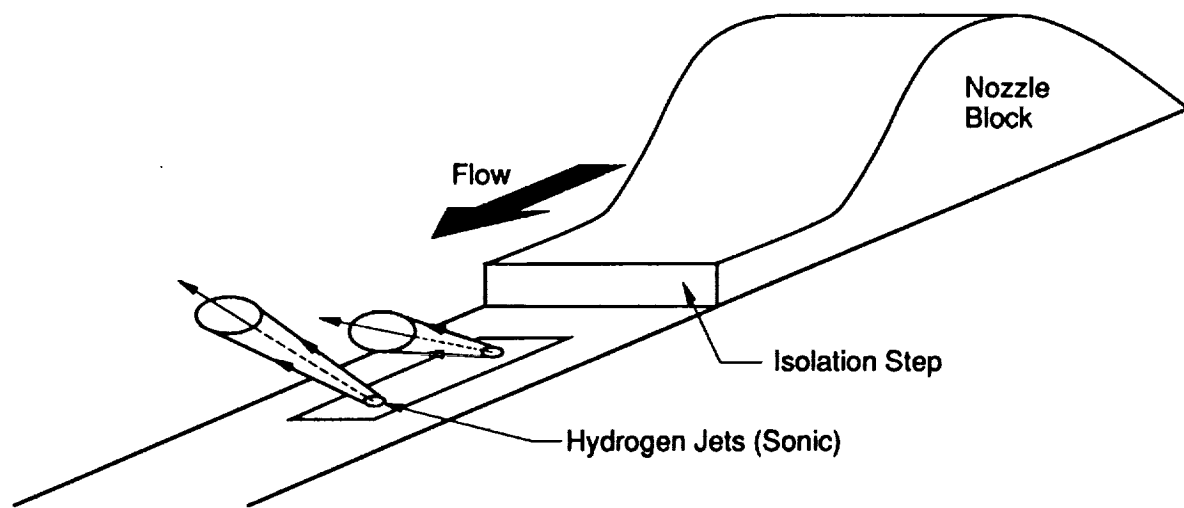


Figure 4. Wall injection system

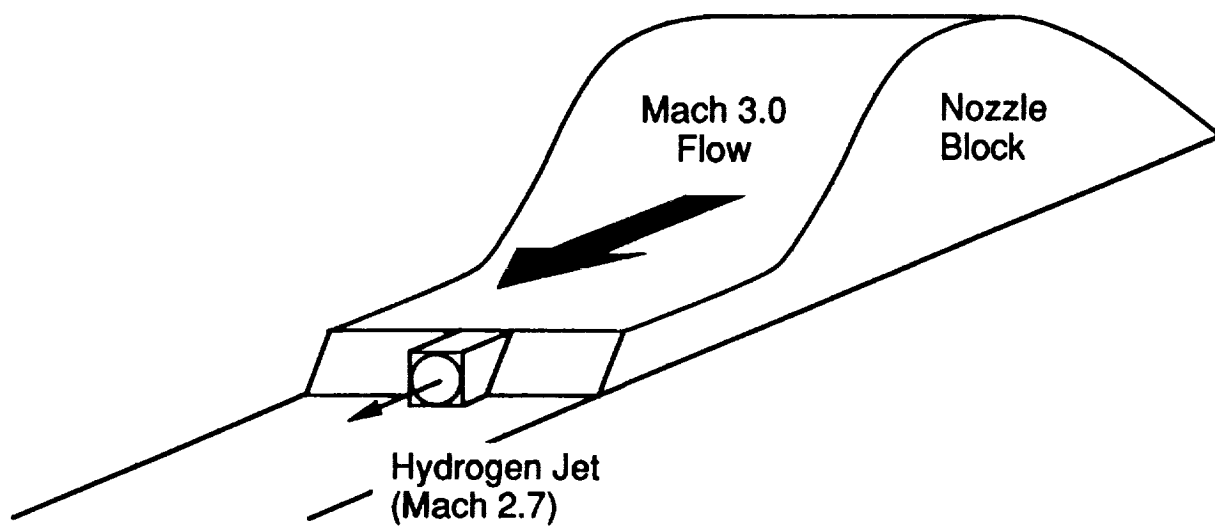


Figure 5. Swept ramp injection system

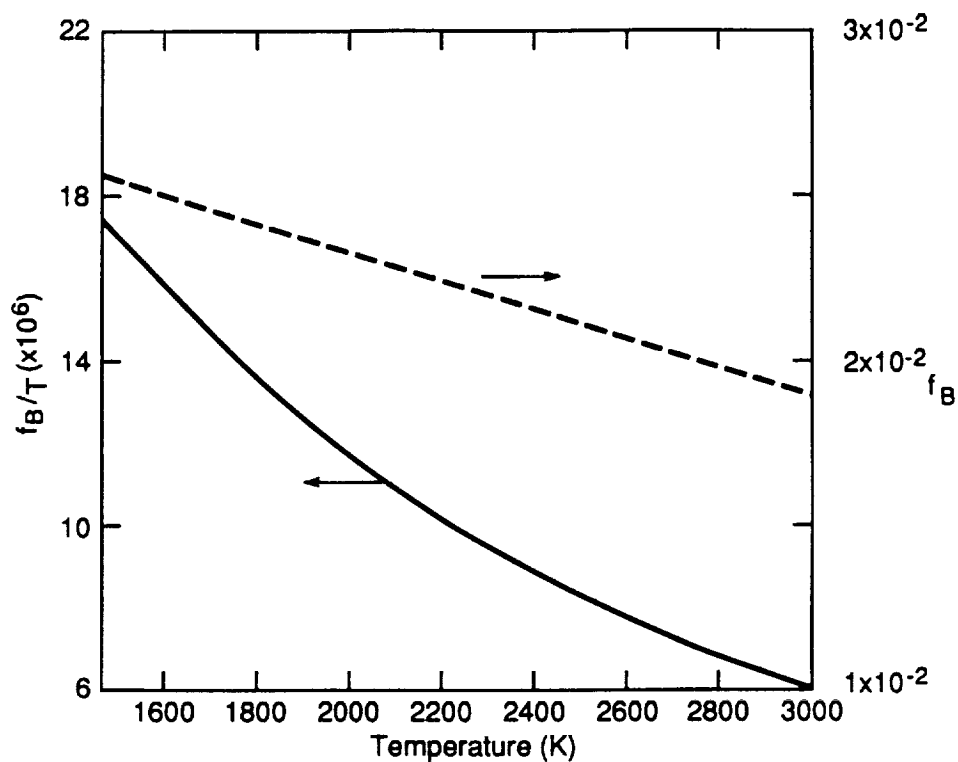


Figure 6. Temperature dependence of the Boltzmann population fraction,  $F_B$ , and the ratio  $f_B/T$  for  $J'' = 7.5$  in OH

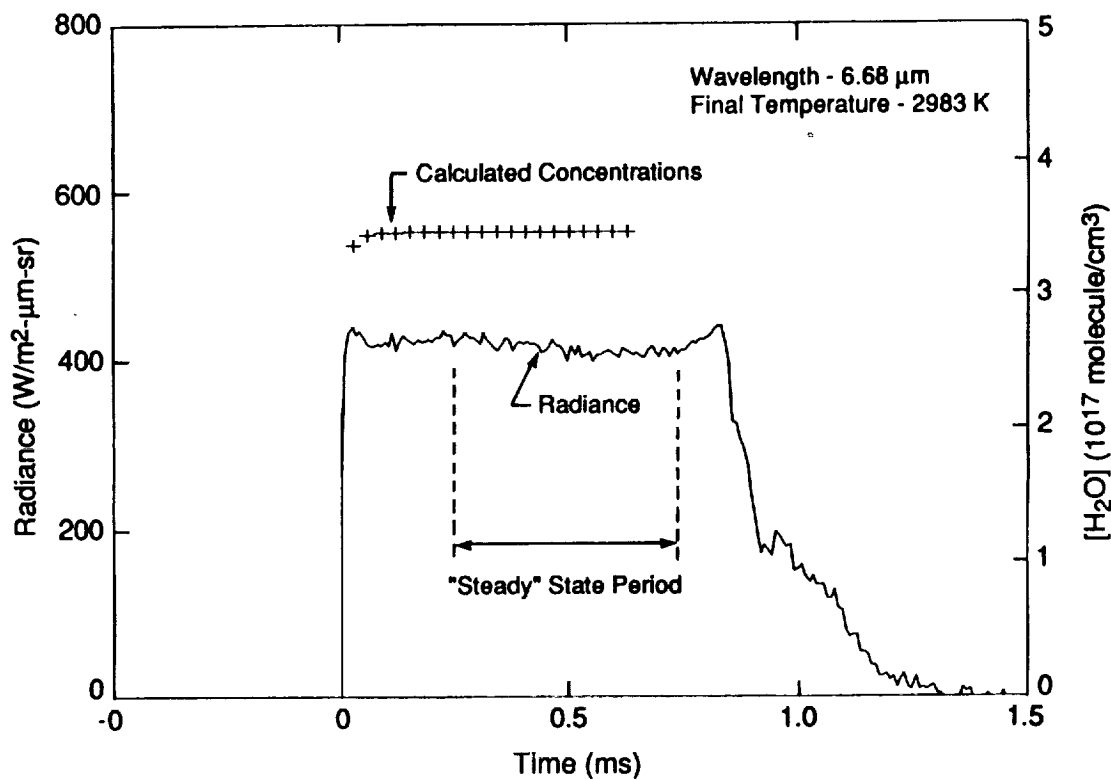


Figure 7. Incident shock tube calibration results and kinetic calculations of  $[H_2O]$

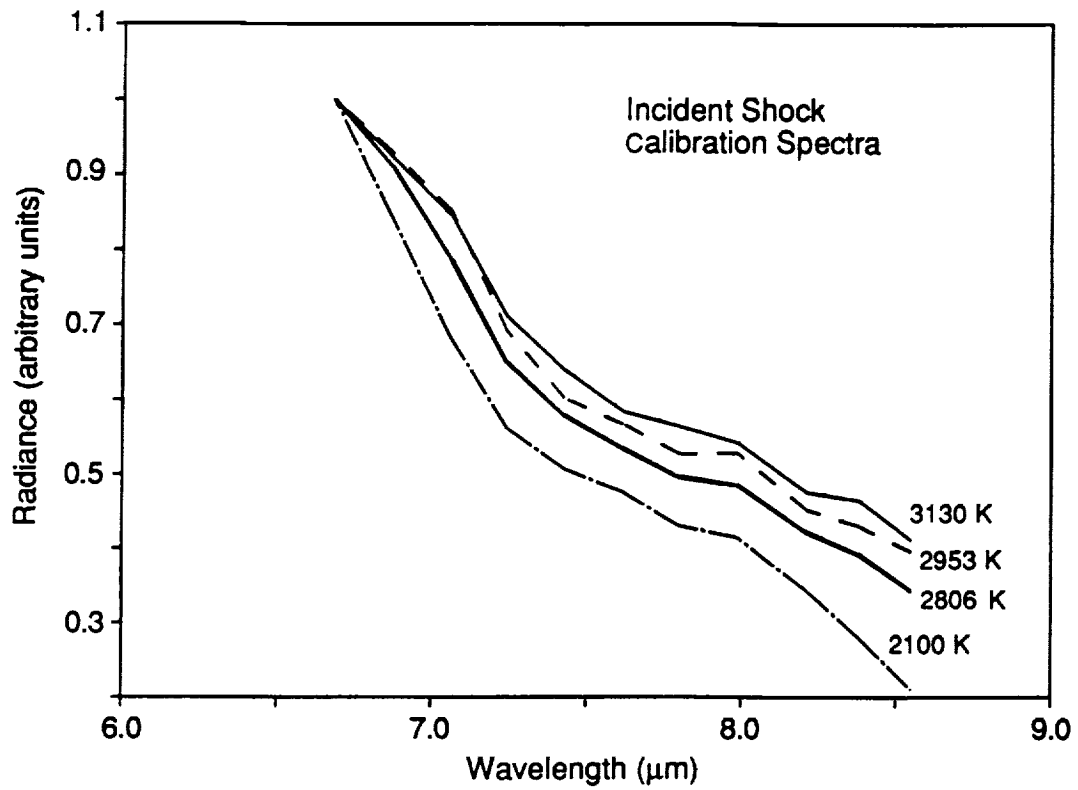


Figure 8. Normalized calibration spectra for water

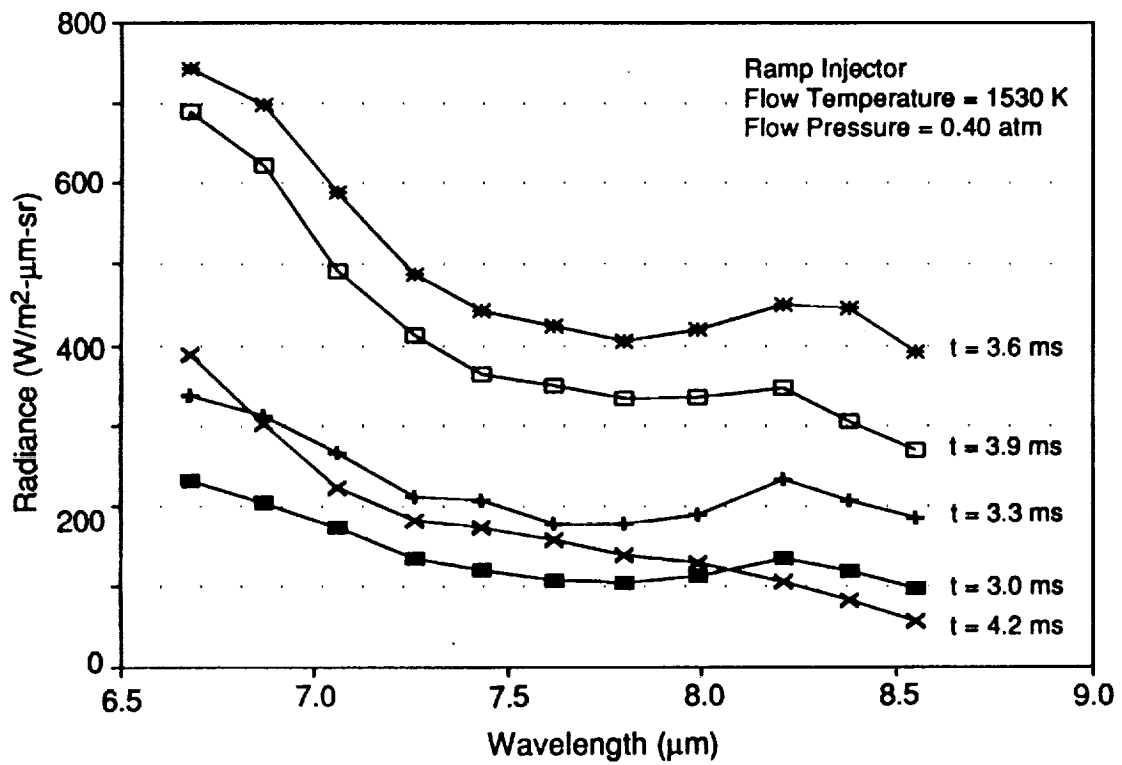


Figure 9. Time resolved spectra from the shock tunnel exit plane

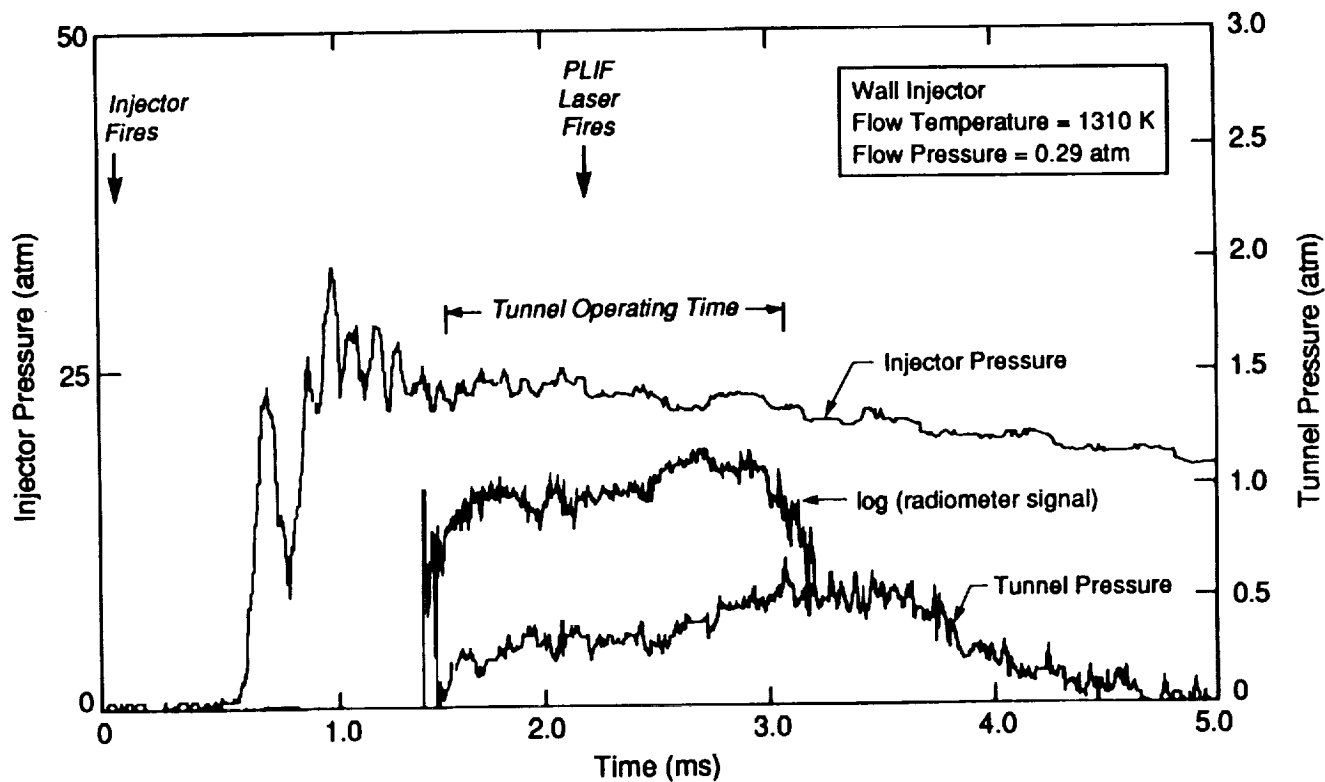


Figure 10. Injection pressure, tunnel pressure, and radiometer signal for a reacting flow measurement

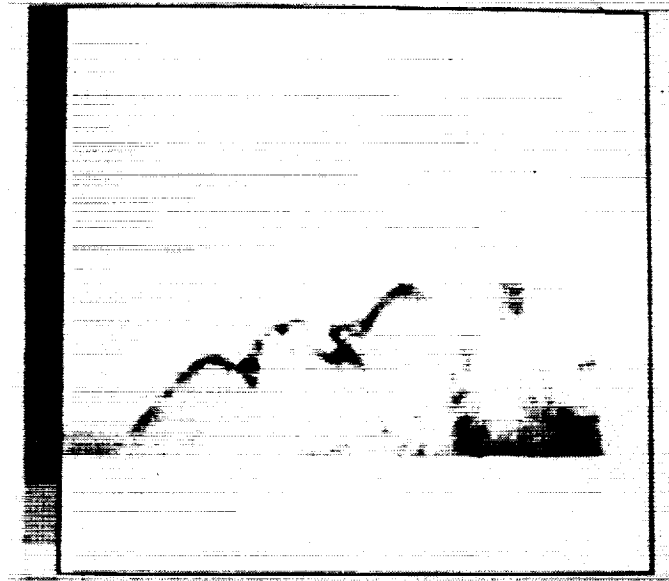


Figure 11. OH PLIF image above the first side wall injector, flow temperature = 1310 K

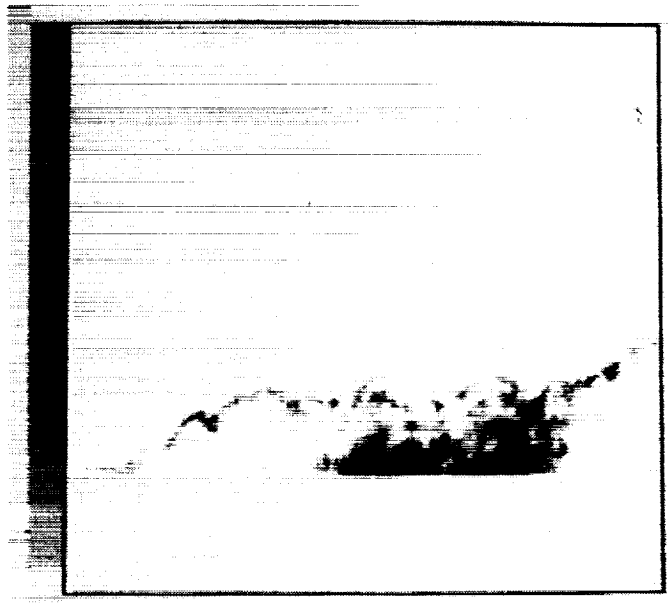


Figure 12. OH PLIF image above both side wall injectors, flow temperature = 1360 K

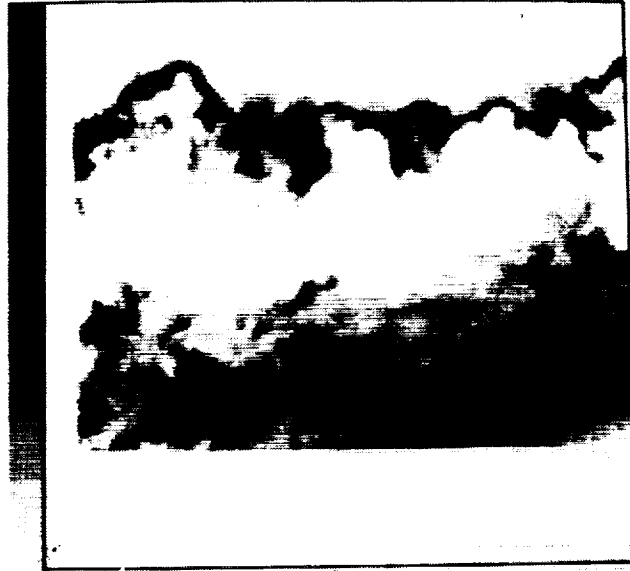


Figure 13. OH PLIF image downstream of axial injector, flow temperature = 1375 K

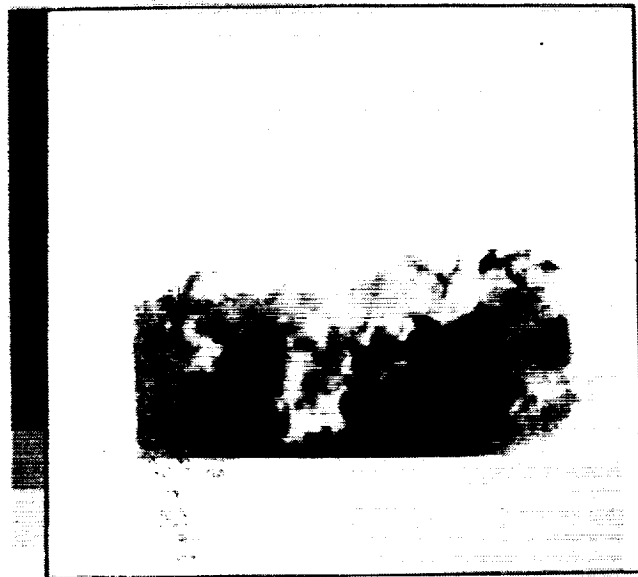
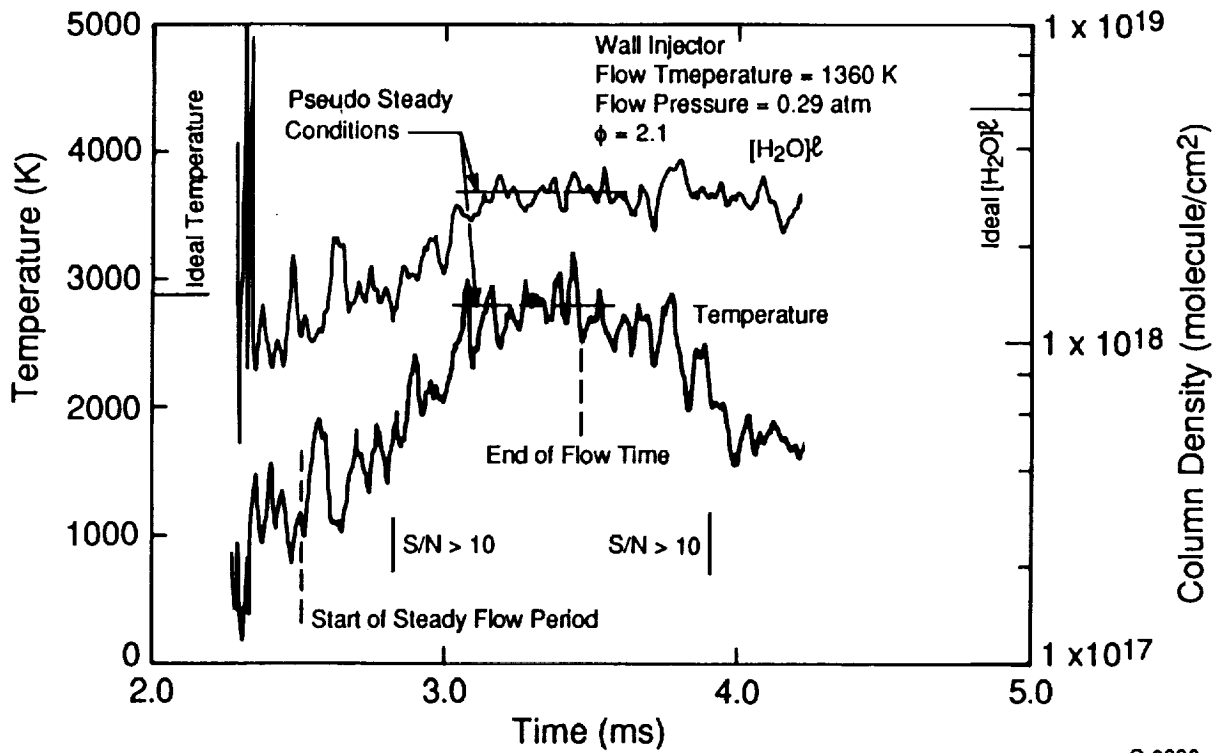


Figure 14. OH PLIF downstream of swept ramp injector with velocity mismatch, flow temperature = 1100 K

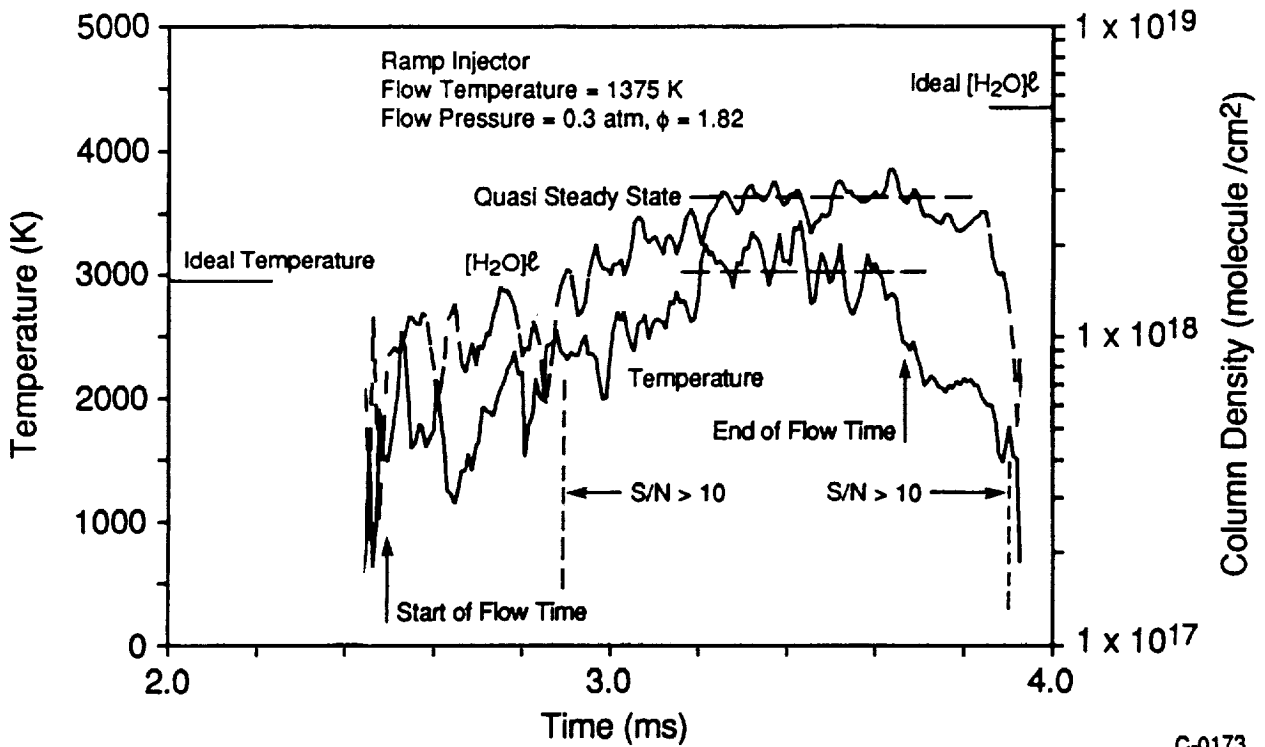


Figure 15. OH PLIF image downstream of swept ramp injector with high speed free stream, flow temperature = 1530 K



C-0339

Figure 16. Wall injection exit plane results



C-0173

Figure 17. Axial injection (with velocity matching) exit plane results





REPORT DOCUMENTATION PAGE			Form Approved OMB No. 0704-0188	
Public reporting burden for this collection of information is estimated to average 1 hour per response, including the time for reviewing instructions, searching existing data sources, gathering and maintaining the data needed, and completing and reviewing the collection of information. Send comments regarding this burden estimate or any other aspect of this collection of information, including suggestions for reducing this burden, to Washington Headquarters Services, Directorate for Information Operations and Reports, 1215 Jefferson Davis Highway, Suite 1204, Arlington, VA 22202-4302, and to the Office of Management and Budget, Paperwork Reduction Project (0704-0188), Washington, DC 20503.				
1. AGENCY USE ONLY (Leave blank)	2. REPORT DATE September 1992	3. REPORT TYPE AND DATES COVERED Conference Proceedings		
4. TITLE AND SUBTITLE The 1992 NASA Langley Measurement Technology Conference: Measurement Technology for Aerospace Applications in High-Temperature Environments			5. FUNDING NUMBERS WU 505-59-54-02	
6. AUTHOR(S) Jag J. Singh and Richard R. Antcliff (Editors)				
7. PERFORMING ORGANIZATION NAME(S) AND ADDRESS(ES) NASA Langley Research Center Hampton, VA 23681-0001			8. PERFORMING ORGANIZATION REPORT NUMBER L-17127	
9. SPONSORING/MONITORING AGENCY NAME(S) AND ADDRESS(ES) National Aeronautics and Space Administration Washington, DC 20546-0001			10. SPONSORING/MONITORING AGENCY REPORT NUMBER NASA CP-3161	
11. SUPPLEMENTARY NOTES Co-sponsors: American Institute for Astronautics and Aeronautics, Washington, DC; The Test Measurement Division and the Aerospace Industries Division of the Instrument Society of America, Research Triangle Park, Raleigh, NC.				
12a. DISTRIBUTION/AVAILABILITY STATEMENT Unclassified-Unlimited Subject Category 35			12b. DISTRIBUTION CODE	
13. ABSTRACT (Maximum 200 words) An intensive 2-day Conference to discuss the current status of measurement technology in the areas of temperature/heat flux, stress/strain, pressure, and flowfield diagnostics for high temperature aerospace applications was held at Langley Research Center, Hampton, Virginia, on April 22 and 23, 1992. Complete texts of the papers presented at the Conference are included in these proceedings.				
14. SUBJECT TERMS Thermocouples; Heat flux sensors; Strain gauges; Rayleigh scattering; Laser speckle; Flowfield diagnostics; Laser-induced fluorescence			15. NUMBER OF PAGES 444	
			16. PRICE CODE A19	
17. SECURITY CLASSIFICATION OF REPORT Unclassified	18. SECURITY CLASSIFICATION OF THIS PAGE Unclassified	19. SECURITY CLASSIFICATION OF ABSTRACT Unclassified	20. LIMITATION OF ABSTRACT	